

Total internal reflection photonic crystal prism

Ethan Schonbrun¹, Maxim Abashin², John Blair³, Qi Wu¹, Wounghang Park¹,
Yeshiahu Fainman², and Christopher J. Summers³

¹Department of Electrical and Computer Engineering, University of Colorado, Boulder, Colorado, 80309
ethan.schonbrun@colorado.edu

²University of California at San Diego, Dept. of Electrical Engineering, 9500 Gilman Drive, La Jolla, CA 92093-0407

³School of Material Science and Engineering, Georgia Institute of Technology, Atlanta, GA, 30332-0245

Abstract: An integrated total internal reflection prism is demonstrated that generates a transversely localized evanescent wave along the boundary between a photonic crystal and an etched out trench. The reflection can be described by either the odd symmetry of the Bloch wave or a tangential momentum matching condition. In addition, the Bloch wave propagates through the photonic crystal in a negative refraction regime, which manages diffraction within the prism. A device with three input channels has been fabricated and tested that illuminates different regions of the reflection interface. The reflected wave is then sampled by a photonic wire array, where the individual channels are resolved. Heterodyne near field scanning optical microscopy is used to characterize the spatial phase variation of the evanescent wave and its decay constant.

© 2007 Optical Society of America

OCIS Codes: (999.9999) Photonic Crystals; (999.9999) Near-field Microscopy; (999.9999) Evanescent waves; (230.5480) Prisms; (230.7390) Waveguides, planar

References and Links

1. D. Axelrod, "Cell-substrate contacts illuminated with total internal reflection fluorescence," *J. Cell. Biol.* **89**, 141-145 (1981).
2. R. C. Reddick, R. J. Warmack, T. R. Ferrel, "New form of scanning optical microscopy," *Phys. Rev. B* **39**, 767-770 (1990).
3. N. J. Harrick, *Internal Reflection Spectroscopy*, (Interscience, New York, 1967).
4. A. Yariv, *Optical Electronics in Modern Communications*, (Oxford, New York, 1997).
5. H. Raether, *Surface plasmons on smooth and rough surfaces and on gratings*, (Springer-Verlag, Berlin, 1988).
6. D. K. Armani, T. J. Kippenberg, S. M. Spillane, and K. J. Vahala, "Ultra-high-Q toroid microcavity on a chip," *Nature* **421**, 925-929 (2003).
7. K. Sakoda, *Optical Properties of Photonic Crystals*, (Springer Series, Berlin, 2001).
8. W. M. Robertson, G. Arjavalingam, R. D. Meade, K. D. Brommer, A. M. Rappe, and J. D. Joannopoulos, "Measurement of photonic band structure in a two-dimensional periodic dielectric array," *Phys. Rev. Lett.* **68**, 2023 (1991).
9. H. Kosaka, T. Kawashima, A. Tomita, T. Sato, and S. Kawakami, "Photonic crystals for micro lightwave circuits using wavelength-dependent angular beam steering," *Appl. Phys. Lett.* **74**, 1370-1372 (1999).
10. Y. Ohtera, T. Sato, T. Kawashima, T. Tamamura, and S. Kawakami, "Photonic crystal polarization splitter," *Electron. Lett.* **35**, 1271-1272 (1999).
11. E. Schonbrun, Q. Wu, W. Park, T. Yamashita, C. J. Summers, "Polarization beam splitter based on a photonic crystal heterostructure," *Opt. Lett.* **31**, 3104-3106 (2006).
12. H. Kosaka, T. Kawashima, A. Tomita, M. Notomi, T. Tamamura, T. Sato, and S. Kawakami, "Self-collimating phenomena in photonic crystals," *Appl. Phys. Lett.* **74**, 1212-1214 (1999).
13. A. Berrier, M. Mulot, M. Swillo, M. Qiu, L. Thylen, A. Talneau, and S. Anand, "Negative refraction at infrared wavelengths in a two-dimensional photonic crystal," *Phys. Rev. Lett.* **93**, 073902 (2004).
14. E. Schonbrun, T. Yamashita, W. Park, and C. J. Summers, "Negative-Index imaging by an index-matched photonic crystal slab," *Phys. Rev. B* **73**, 195117 (2006).
15. B. Momeni, J. Huang, M. Solatani, M. Askari, S. Mohammadi, M. Rakhshandehroo, and A. Adibi "Compact Wavelength Demultiplexing Using Focusing Negative Index Photonic Crystal Superprisms," *Opt. Express* **14**, 2413 (2006).

16. T. Yamashita and C. J. Summers, "Evaluation of Self-Collimated Beams in Photonic Crystals for Optical Interconnect" *J. Select. Areas. Commun.* **23**, 1341 (2005).
17. Z. Ruan, M. Qiu, S. Xiao, S. He, and L. Thylen, "Coupling between plane waves and Bloch waves in photonic crystals with negative refraction," *Phys. Rev. B.* **71**, 045111 (2005).
18. W. Park, "Modeling of photonic crystals" in *Handbook of Theoretical and Computational Nanotechnology Vol. 7*, ed. by M. Rieth and W. Schommers (American Scientific Publishers, Stevenson Ranch, CA, 2006), pp. 263-327.
19. B. Lombardet, L. A. Dunbar, R. Ferrini, and R. Houdre, "Fourier analysis of Bloch wave propagation in photonic crystals" *J. Opt. Soc. Am. B* **22**, 1179-1190 (2005).
20. I. De Leon and F. S. Roux, "Fourier analysis of reflection and refraction in two-dimensional photonic crystals" *Phys. Rev. B* **71**, 235105, (2005).
21. M. L. M. Balisteri, J. P. Korterik, L. Kuipers and N. F. van Hulst, "Local Observations of Phase Singularities in Optical Fields in Waveguide Structures" *Phys. Rev. Lett.* **85**, 294 (2000).
22. P. Tortora, M. Abashin, I. Märki, W. Nakagawa, L. Vaccaro, M. Salt, H. P. Herzig, U. Levy, and Y. Fainman "Observation of Amplitude and Phase in Ridge and Photonic Crystal Waveguides Operating at 1.55 μm by Use of Heterodyne Scanning Near-Field Optical Microscopy," *Opt. Lett.* **30**, 2885 (2005).
23. E. Schonbrun, Q. Wu, W. Park, T. Yamashita, C. J. Summers, M. Abashin and Y. Fainman, "Wave front evolution of negatively refracted waves in a photonic crystal" *Appl. Phys. Lett.* **90**, 041113 (2007).

1. Introduction

The presence of an evanescent field is the signature of near-field optics. There are two main characteristics of these waves that distinguish them from propagating waves. The first is their intensity profile, which exponentially decays away from the source that created them. This means that they are highly localized to a surface or edge. In microscopy [1, 2] and spectroscopy [3], this results in a method of depth sectioning, which adds increased resolution and specificity. Another benefit of evanescent illumination is that it is a dark field method in that the background illumination does not reach the collection optics, resulting in larger signal contrast. Evanescent waves in this context are most often created with a free space total internal reflection (TIR) prism illuminated above their critical angle. A second characteristic of evanescent waves is that they carry a larger spatial frequency than propagating waves can support in their medium. This feature allows them to externally couple to bound modes of other structures. On integrated platforms, the evanescent field in the cladding of a waveguide has been most often used for coupling. A large disadvantage of using this geometry is that the spatial frequency is fixed by the cladding index and the waveguide propagation constant, where as a TIR prism can generate a range of spatial frequencies by changing the optical wave's incident angle. Excitation of bound modes has applications in waveguide coupling [4], plasmonics [5], and high Q resonators [6].

In this paper, we demonstrate a photonic crystal (PC) TIR prism that can operate at small incident angles or even normal incidence. An evanescent wave is generated along the interface and exponentially decays into the air region behind the PC. The reflected wave has close to unity magnitude owing to the odd symmetry of the incident Bloch mode [7]. The inverse situation has previously been studied, where a wave incident from free space is totally reflected back into air and consequently the Bloch mode has been called an "uncoupled mode" [8]. Unlike in the photonic band gap, a mode at this frequency and momentum does exist in the PC however; it is the coupling across the interface that is forbidden. In the presented TIR prism design, a Bloch mode is excited inside the PC across an allowed interface and then is reflected at a forbidden interface. Using the Fourier spectrum of the Bloch mode, we show that a tangential momentum matching condition in the extended zone scheme describes this effect.

PCs have previously been used in the design of prisms that sort an incident wave based on its spectrum [9] or polarization state [10-11]. These devices utilize the anomalous dispersive properties of Bloch waves in PCs. Although there is no transverse confinement in PC prisms, the diffraction of an optical beam can be controlled by using either the self-collimation [12] or the negative refraction effect [13, 14]. This leads to a device that can beat

the normal scaling rules for free space optics [15]. For devices operating in this anomalous diffraction regime, an input beam can have a width of just a few wavelengths and can maintain this size through a region several Rayleigh ranges long. One advantage of integrated devices without transverse confinement is that they can support several parallel channels that can pass through one another similar to a free space optical device [16]. Because the total internal reflection occurs in the second photonic band where slow or negative diffraction also occurs, the PC TIR prism also takes advantage of this parallelism.

2. Bloch wave coupling

In order for a PC Bloch wave to be efficiently excited at a crystalline interface, the incident field has to have a large spatial overlap with the Bloch wave field profile. Bloch modes originating from higher photonic bands can have a complex field profile containing several peaks and nodes in each unit cell. This fact makes coupling to higher photonic bands a complex and inefficient process that can limit the functionality of devices that use them in their design. Propagation in the second photonic band of a two dimensional hexagonal lattice of circular air holes has received a lot of attention due to the presence of negative refraction in this regime. Theoretical and numerical studies have shown that waves incident from vacuum can couple efficiently into this structure when the interface has its normal in the ΓM direction, while the coupling is close to zero when the interface has its normal in the ΓK direction [17]. In this paper, we use the inability of this mode to couple across the ΓK interface as an efficient internal mirror in the design of a reflection prism.

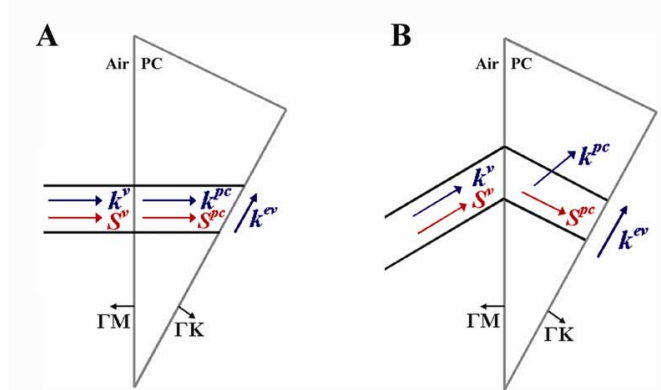


Fig. 1. Photonic Crystal total internal reflection prisms. The prism is a triangular lattice of holes and the incident medium is air. If a mode in the second photonic band is excited, the wave can couple into the prism through the ΓM interface, but not out the ΓK interface. A) shows a beam normally incident into the prism, where the excited Bloch wave has parallel momentum, k^{pc} , and Poynting, S^{pc} , vectors. The energy of the wave is then obliquely incident into the reflection interface. B) shows a beam obliquely incident into the PC that negatively refracts across the boundary. The Bloch wave has a large angle between its k^{pc} , which bends positively, and S^{pc} , which bends negatively. The energy of the wave is normally incident into the reflection interface, yet still experiences TIR.

In the simplest implementation, an optical beam is normally incident into the hypotenuse of a $30^\circ\text{-}60^\circ\text{-}90^\circ$ prism, which has a ΓM interface, as shown in Fig. 1(A). Inside the PC, a Bloch mode is excited that propagates in the ΓM direction and is subsequently incident at 30° into a ΓK interface. Using a folded value of the Bloch wave momentum k^{pc} , the magnitude of the effective index of the mode, defined as $|k^{pc}/k^v|$, where k^v is the wave momentum in vacuum, is approximately unity in the second photonic band. With this value of an index, light is expected to refract across the ΓK interface because the incident angle is well below the critical angle. The fact that instead almost no light couples out has been explained by

considering the symmetry properties of Bloch waves [7, 8, 18]. It is also possible to describe this reflection by a momentum conservation condition across the boundary using the unfolded Bloch wave vector. When the index contrast of a PC is large, a Bloch wave is composed of a superposition of a large number of plane wave components [19]. In the case considered here, the excited mode lies in the middle of the band and although there are several plane wave components present, the majority of the energy lies in a single neighboring reciprocal lattice unit cell. The Bloch wave vector of this component cannot match across an interface with vacuum at 30° incident angle and consequently experiences TIR. The full Bloch wave spectrum and momentum matching will also be discussed in the next section.

If the input optical beam is deflected so that it is incident at a 30° angle, a Bloch wave propagating in the ΓK direction is excited, as shown in Fig. 1(B). In this case, the energy bends negatively and is pointed in the ΓK direction due to the strong anisotropy of the unfolded equi-frequency surface (EFS). Conversely, the Bloch wave vector bends only a small amount in the positive direction. The Bloch wave energy is normally incident onto the ΓK interface, yet it still undergoes TIR. The reason for this is that the wave vector has an even larger angle with respect to the interface normal than in the case of Fig. 1(A). The transverse wave vector is in fact larger for the case in Fig. 1(B) than in Fig. 1(A) as shown by the longer arrow in the figure. This example clearly shows the importance of using the unfolded Bloch wave vector for phase sensitive experiments, such as coupling across an interface.

3. Design and simulation

Although the reflection in Fig. 1(B) is more surprising in nature, we chose to fabricate a device based on Fig. 1(A) because it allows access to the reflected beam. The PC region was symmetrically reflected along the short leg of the right triangle to form a 120° - 30° - 30° prism where light enters and exits a ΓM -to-silicon interface and is reflected from a ΓK -to-air interface, as shown in Fig. 2(A). Small regions around each 30° vertex have been removed because they do not substantially effect light propagation. Three input waveguides each of which is $3\ \mu\text{m}$ wide and separated from each other by $5\ \mu\text{m}$, terminate $68\ \mu\text{m}$ from the PC prism, as shown in the lower right of Fig. 2(A). Light couples into a PC mode in the second photonic band where the EFS is flat along the ΓM direction. The beam then propagates with minimal diffraction for $22\ \mu\text{m}$ in the PC, reflects off the ΓK interface and propagates through another $22\ \mu\text{m}$ inside the prism before coupling back out to the silicon slab. The output beam is sampled by a photonic wire array of $1\ \mu\text{m}$ wide wires with center-to-center spacing of $3\ \mu\text{m}$.

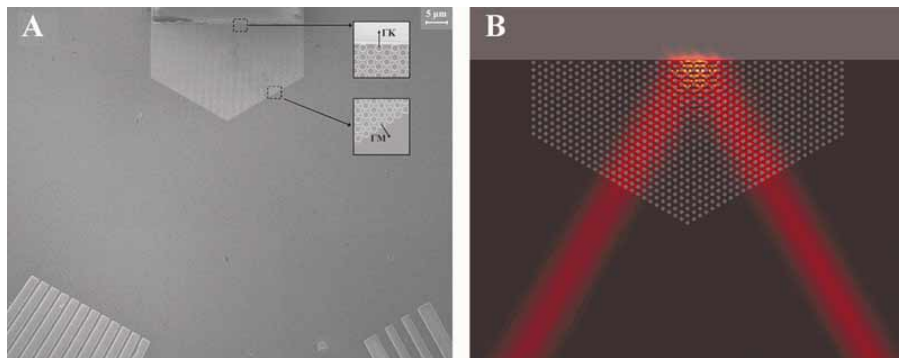


Fig. 2. A) Scanning electron micrograph (SEM) of the fabricated device. The insets show the crystal terminations for the prism input and reflection interfaces. The front half of the prism is surrounded by silicon slab, and behind the prism is an etched out air trench. B) Numerical simulation of the time averaged square of the E_z (out-of-plane) field. The wave is incident from the bottom right and exits the bottom left. The numerically simulated device is three times smaller than the fabricated device, so diffraction is negligible.

Figure 2(B) shows a two-dimensional (2D) finite difference time domain (FDTD) simulation of a version of the PC prism that is one-third size of the fabricated sample. The image shows the optical intensity of a TM wave, E field is perpendicular to the substrate, traveling through the device. The PC is composed of 300 nm diameter circular air holes in a hexagonal lattice with a lattice constant of 510 nm in a 300 nm device layer silicon-on-insulator (SOI) platform [14]. At an incident wavelength of 1550 nm, the effective index of the fundamental TM mode in the Si device layer is 2.54. From the FDTD simulation, the magnitude of the reflected wave at the input interface of the prism appears to be very small as seen by the barely visible fringe modulation depth in the input arm. The beam in the PC propagates in the negative refraction regime and forms an internal focus at the reflection edge, and has an external image at the output waveguide array. However, because of the hexagonal distortion that flattens the EFS in the Γ M direction which is typically observed in a triangular PC, diffraction is small and the image plane is difficult to resolve. As the size of the prism increases, diffraction management becomes increasingly more important in order to achieve a large number of resolvable spatial channels in the device and to keep the transverse size of the beam small at the reflection interface.

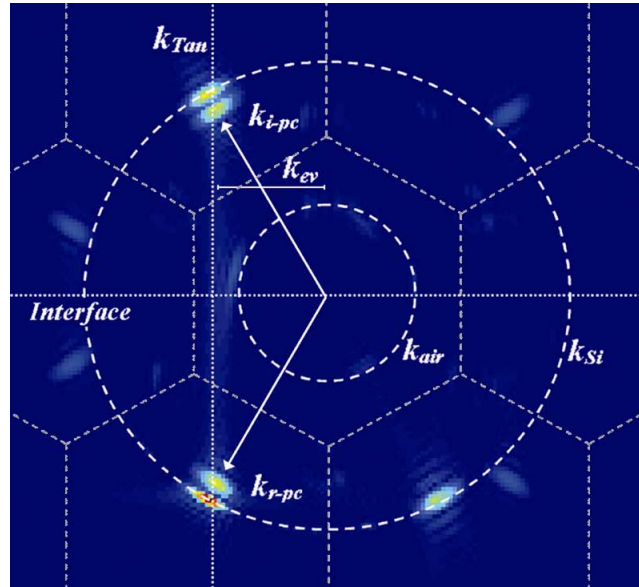


Fig. 3. The Fourier spectrum of the numerically simulated complex field. The spectrum has five major components, the incident, reflected, and transmitted waves on k_{Si} , the incident Bloch wave k_{i-PC} , and the reflected Bloch wave k_{r-PC} . The energy of the incident k_{Si} and k_{pc} waves travel towards the upper left and the energy of the reflected k_{Si} and k_{pc} waves travel towards the lower left similar to Fig. 2(B). The evanescent wave spectrum lies just beyond the k_{air} circle and is difficult to resolve in this figure because the wave only occupies a small fraction of the area in real space. Most of the energy in the incident and reflected Bloch waves is carried by the indicated unfolded EFS in the neighboring reciprocal lattice cells. Other EFS harmonic components are significantly weaker.

To describe the momentum matching conditions more completely, we analyze the spectrum of the field data obtained through FDTD [20]. Figure 3 shows the Fourier transform of the complex electric field obtained with the same parameters as Fig. 2(B). The spectrum represents the momentum distribution in the input and output silicon slab regions, the PC prism, and the air trench behind the reflection plane. Three bright regions on the k_{Si} -surface show the incident, reflected, and output light. The radius of the k_{Si} -surface is $2.54k_{air}$ due to the effective index given to silicon for TM polarization. The primary Bloch wave momentum

distributions, designated by arrows for the incident and reflected waves, are located very close to the silicon slab mode. This explains the small reflections at the silicon PC interfaces, estimated to be as low as 2 percent. Secondary EFS surfaces are visible in the spectrum, but their Fourier amplitude is much smaller than the primary surfaces. Almost no energy is present in the first Brillouin zone (FBZ), which further shows that momentum matching across a boundary should not use the folded values only.

The tangential momentum of the incident Bloch wave impinging on the TIR interface is shown in Fig. 3 by the vertical dotted line and dictates the magnitude of the momentum of the evanescent wave, k_{ev} . Because of the momentum distribution of the incident Bloch wave, only a small fraction of the energy is able to couple across the boundary and excite a propagating wave in the air trench. The peak value of $k_{ev} = 1.2k_{air}$ and consequently cannot be matched and experiences TIR. If we imagine rotating $k_{i,PC}$ five degrees counterclockwise, which would be caused by a five degree incident angle into the PC from the silicon, the behavior is similar to Fig. 1(B). The Bloch mode energy is now on the adjacent corner of the hexagonal EFS. The direction of energy flow changes by 30° and is now normally incident into the interface, but $k_{i,PC}$ has a larger transverse momentum than the previous case and thus even more efficiently TIRs. Using the knowledge that the primary EFS surface is not the one in the FBZ for modes in the second photonic band, the inability to couple across the ΓK boundary can be explained by transverse momentum conservation as well as the mode symmetry.

4. Far-field characterization

Using an objective lens, scattered light from the different interfaces is collected and imaged onto an infrared camera. Far-field scattered light does not give detailed information on the generated evanescent wave or low loss guided regions, but lets us track intensity through the integrated optical system. Scattered intensity is useful for rough estimates on the transmission coefficient of the PC prism and for monitoring the beam width at the output. Figure 4 shows four far-field images of the device, where Fig. 4(A/C) is with 1542 nm TM/TE illumination, and Fig. 4(B/D) is with 1559 nm TM/TE illumination. In each figure, the input waveguides are at the top left, where the light is moving from left to right. The guided optical wave is then reflected by the prism where it is finally incident on the output waveguide array located at the bottom of each figure. Figure 4(A) represents the wavelength which displays the tightest field confinement shown by the small field distribution incident on the output waveguide array. Figure 4(B) shows the wavelength where reflection losses are the lowest shown by the brightness of the output spot. Although all three terminations of the input waveguides light up, the scattered light does not represent the field in each input waveguide. This scattered light is from the sharp edges of the termination and could be reduced with an inverse taper.

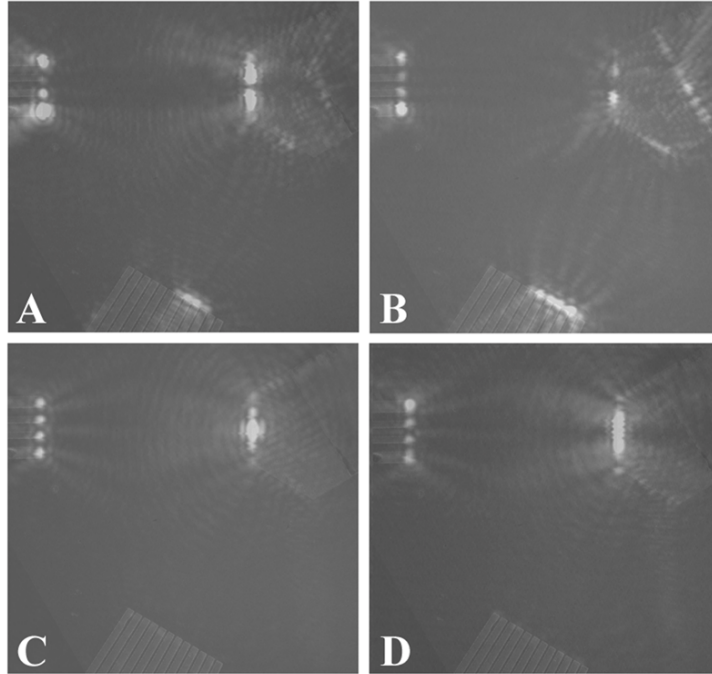


Fig. 4. Far-field scattering images of the PC prism. The center input waveguide is illuminated. The scattering images are superimposed on an SEM image to show the device geometry. In each photograph, the input waveguide is at the upper-left, the TIR prism is in the upper-right and the output waveguide array is along the bottom. A) shows 1542 nm TM polarized illumination, which creates a highly confined output spot that primarily illuminates two output waveguides. B) shows 1559 nm TM polarized illumination, which has high efficiency and small out-of-plane scattering at each device interface. Scattering from the output waveguide array is significantly brighter than any other region indicating the small losses at the other interfaces. C, D) show 1542 and 1559 nm TE polarized illumination respectively, which does not couple into the PC prism.

The images in Fig. 4 represent the response when only the middle input waveguide is excited. The field distribution in the $3\ \mu\text{m}$ input guides has a half width at e^{-1} value of $1.19\ \mu\text{m}$ and $1.14\ \mu\text{m}$ for TM and TE respectively. Using a gaussian beam model for propagation, the Rayleigh range (z_0) for the TM mode is $7.44\ \mu\text{m}$ and $8.08\ \mu\text{m}$ for the TE mode. The distance from the termination of the input guide to the start of the output photonic wire array in the folded optical system is $180\ \mu\text{m}$, which is more than $20z_0$. The wave propagates $68\ \mu\text{m}$ from the input guide to the prism edge, where it diffracts to a full width of $22\ \mu\text{m}$ for TM and $19\ \mu\text{m}$ for TE. The e^{-1} points of the beam just fit into the aperture of the prism, which is $24\ \mu\text{m}$ wide. From Fig. 4(A, C), the TM mode looks slightly larger than the TE mode when it is incident on the prism and is roughly the width of the input interface, which matches the prediction. The beam then propagates through the PC prism in a slow diffraction regime with a small amount of negative curvature, which contracts the beam size. After reflection and propagation through the second silicon slab region, the beam is incident onto the output photonic wire array, where we can measure its transverse size. At the tightest confinement where diffraction is most effectively managed, shown in Fig. 4(A), the beam has a full width of $7\text{-}10\ \mu\text{m}$, which is roughly half the size as it was on the prism entrance and $1/24$ of the size it would be if it propagated through $180\ \mu\text{m}$ of uniform silicon slab. The TE mode is effectively filtered out of the system as can be seen from the small amount of light reaching the output in Fig. 4(C, D). The image in Fig. 4(B) shows how efficient the PC prism can be, where the amount of light hitting the output waveguide array is much stronger than the scattered signals at the other interfaces. Numerically, the device is predicted to transmit up to

95% of the light, and though this number is not verified experimentally, the efficiency appears to be high.

When each of the incident waveguides is selectively excited, the response of the system can be studied for each spatial channel. Figure 5 shows the intensity profile at the beginning of the photonic wire array at 1542 nm. The black dashed line represents the calculated intensity distribution of the beam after traveling through 180 μm of unpatterned silicon slab. The widths of the output beams are 7-10 μm for each of the spatial channels, which is on the same order as their spatial separation, which is 6 μm given by the separation between the input waveguides. Although there is some cross-talk between the channels, they are spatially resolved. The resolvability can be considerably increased in the future by shortening the silicon slab regions. This result, however, shows the capability of diffraction management using a Bloch mode in the second photonic band.

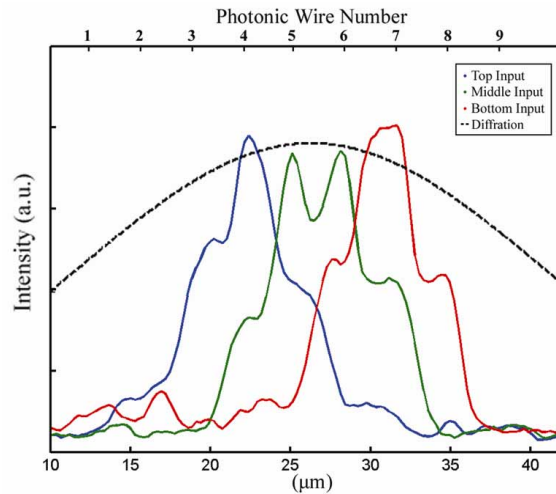


Fig. 5. Cross-section of the output photonic wire array for excitation of each input waveguide. The diffraction curve is calculated with a gaussian beam model and is normalized to the peak height of the other curves.

5. Near-field characterization

Using a heterodyne near-field scanning optical microscope (HNSOM) [21-23], we measured the amplitude and phase of the guided wave at the reflection interface. Figure 6(A) and its inset on the right show that the amplitude image of the detected field has a peak at the interface and then exponentially decays into the air trench, while staying at a roughly constant value in the PC. The wavelength of illumination is 1552 nm, which does not give the tightest field confinement at the interface, but gives a strong signal showing a bright evanescent field. The phase of the field in Fig. 6(B) shows that along the reflection interface, the phase varies only in the tangential direction. An evanescent field's momentum vector is real only for the direction parallel to the interface, so the phase should not progress in any other direction. The inset shows a cross-section of the phase 260 nm behind the interface that has a period of 1.42 μm , which is below the free space wavelength, indicating that the wave is evanescent.

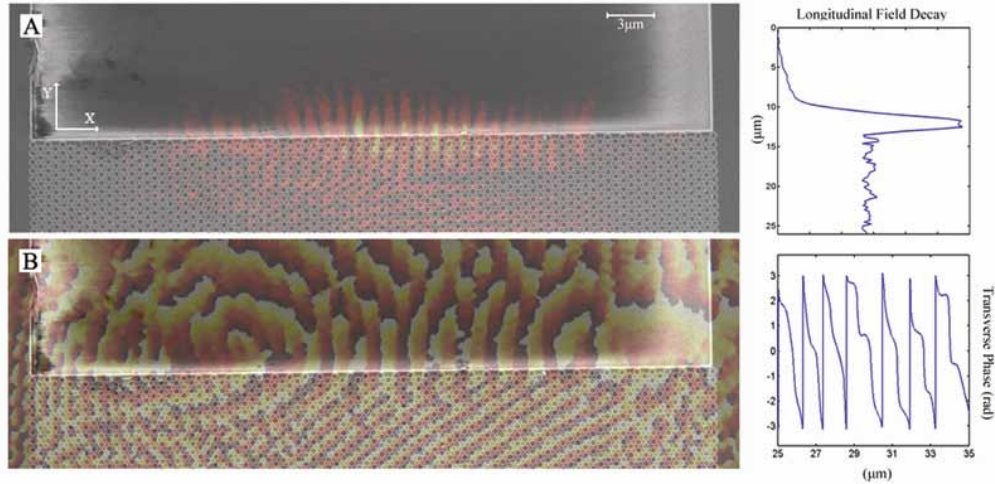


Fig. 6. The amplitude and phase images along the reflection interface collected by the HNSOM superimposed on the SEM image to show the geometry. The inset to the amplitude image shows the field amplitude averaged over a $10\ \mu\text{m}$ cross-section plotted vs. Y . The inset to the phase image shows the evanescent field phase one sample above the interface in the air region plotted vs. X .

The decay constant of the evanescent field is measured to be $1.20\ \mu\text{m}$, defined as the e^{-1} location of the field amplitude. The inset is obtained by summing a $10\ \mu\text{m}$ wide field along the boundary, and plotting the summation as a function of vertical distance along Y . The summation averages field values over several unit cells of the PC and results in a smooth curve. Field values in the HNSOM image are sampled at an interval of $260\ \text{nm}$, so there are 4-5 measurements in the e^{-1} decay region. A near-field object is convolved with the collection tip, in this case $200\ \text{nm}$. This convolution blurs sharp features by approximately this amount, which increases the measured decay distance. Along the interface, the amplitude is modulated by the surface periodicity of the PC, $\sqrt{3}a$, but this does not describe the phase progression along the TIR interface, as we will see by looking at the tangential phase profile.

The phase image in Fig. 6(B) shows a coherent wave incident into the boundary from the PC and along the interface. The tangential momentum of these two waves is equal according to the boundary condition. By taking a cross-section of the phase image just beyond the interface in the air region, the spatial period of the wave is observed to be $1.42\ \mu\text{m}$, which gives $k_{ev}=1.09k_{air}$. The decay constant of an evanescent wave can be predicted from its momentum by the expression $D = 1/\sqrt{k_{ev}^2 - k_{air}^2}$. Using $k_{ev}=1.09k_{air}$, the decay constant is expected to be $570\ \text{nm}$, which is smaller than the measured value of $1.2\ \mu\text{m}$. Because the field is spatially confined, there is a spectrum of transverse momentum values at the boundary. Lower spatial frequencies decay slower into the air region, so they have greater influence at large distances from the interface. In order to better understand the spectrum of the evanescent wave, we perform Fourier analysis of the measured complex field. This method also gives insight into the reason for measuring a larger D .

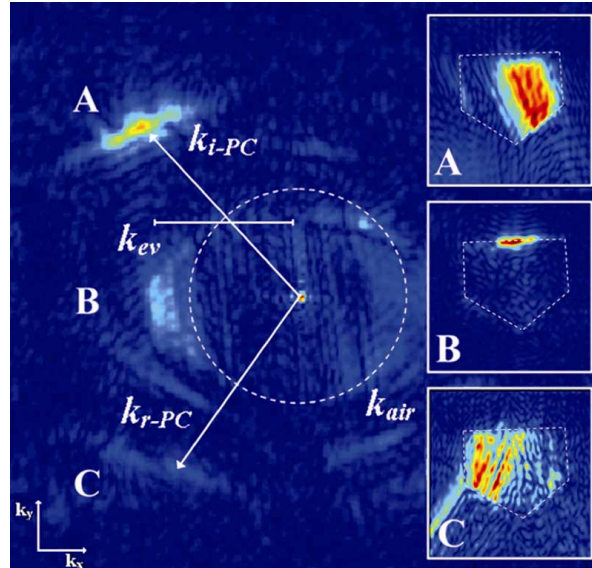


Fig 7. The Fourier spectrum of the complex field values collected by the HNSOM. The arrows show the incident Bloch wave, k_{i-PC} , the reflected Bloch wave, k_{r-PC} , and the evanescent wave, k_{ev} . The dotted circle shows the air light line at 1552 nm. The insets show the windowed regions after being inverse transformed back to the spatial domain, a dotted line outlines the prism.

Figure 7 is the numerical Fourier transform of the measured complex field from a $15 \times 15 \mu\text{m}$ scanning area centered at the reflection edge. The figure is similar to Fig. 3, except that the field of view contains only the PC region and the air trench behind the reflection interface. The brightest feature in the spectrum is the incident Bloch wave, k_{i-PC} , and is located in the upper left region indicating that its phase progresses in that direction. By measuring the magnitude of k_{i-PC} , the effective index of the primary momentum distribution is estimated to be 2.2. As long as this value is larger than 2.0, the Bloch wave will TIR at the boundary when the incident angle is 30° , as it is in the prism. This value agrees with the numerical prediction from FDTD of 2.35 and further illustrates the close momentum match between the PC mode and the slab mode, which has an index of 2.54. It is also evident that the momentum distribution is flat indicating that the wave is in a slow diffraction regime. This region of the spectrum is labeled A.

At the same tangential momentum, but along the k_x -axis, is the second brightest region labeled B. The spectrum of the evanescent wave is expected to be in region B because the only real component of its momentum is along the tangent of the interface. From the figure, the evanescent spectrum lies just beyond the air light line and extends from $1.0k_{air}$ to $1.3k_{air}$. The momentum components only slightly larger than k_{air} will decay more slowly and are responsible for the larger than expected measured value of D. The higher end of the k_{ev} spectrum compares well with the value expected by numerical simulation. Region C contains the reflected wave spectrum.

Each region can be windowed and inverse Fourier transformed back to the spatial domain to view where that part of the spectrum is located. The inset labeled A shows that this region is in fact the incident PC mode, which starts at the PC input facet and ends at the reflection interface. Region C, though weaker, shows the reflected PC wave starting at the reflection interface and ending at the PC output facet. Region B, which is the evanescent wave, is confined to the reflection edge. The windowed spatial field distribution has less resolution, but makes it possible to isolate different components of the detected field. The near-field

microscope more efficiently collects the PC prism's evanescent field as can be seen by the low noise floor in inset B compared to the other insets.

6. Conclusion

A PC TIR prism has been demonstrated that acts as an efficient evanescent wave source and is integrated onto a silicon platform. Different resolvable regions along the PC to air boundary can be selectively addressed due to diffraction management. These channels spatially overlap in the prism so consequently perform a function that is difficult to obtain in conventional integrated waveguides. The device can in the future be scaled up to accommodate more channels, since the number of resolvable channels is determined by the aperture of the prism divided by the beam size, which can be on the order of $1-2 \lambda$. In addition, the near-field performance of this device has been characterized. We have directly measured the phase and amplitude distributions of the generated evanescent wave. By analyzing the spectra of the complex field, we have presented experimental results that show the tangential momentum mismatch across the reflection boundary. The strong presence of the detected evanescent fields, ability to exhibit TIR at small angles and the unique diffraction management schemes, make the PC TIR prism an efficient and flexible platform for achieving evanescent wave coupling, imaging, and sensing functionalities in an integrated photonics environment.

Acknowledgments

This work is supported in part by the National Science Foundation (DMI-0304650, BES-0608934) and the Army Research Office (W91NF-06-1-0377). CJS and JB thank the Georgia Tech MiRC cleanroom staff for their valuable assistance.